

Pose-aware C-Arm Calibration and Image Distortion Correction for Guidewire Tracking and Image Reconstruction

Florian Heemeyer^{1,2}, Anirudh Choudhary¹ and Jaydev P. Desai, *Fellow IEEE*

Abstract—Image intensifiers, also known as C-arms, are important and low-cost tools for surgeons to guide minimally-invasive procedures. However, image intensifiers suffer from several distortions that can impede their ability to provide accurate guidance. These distortions can be misleading during an automated minimally-invasive surgery where the accurate shape-estimation of the robot is essential. Since the distortion strongly depends on the orientation of the C-arm during image acquisition, we propose an approach for distortion correction in combination with a calibration procedure to precisely estimate its orientation. To estimate an accurate distortion correction function, we take images of a calibration grid in 258 different C-arm orientations and apply polynomial regression on these images. The C-arm is calibrated using an external camera along with optical flow and point-correspondence-based matching to allow sufficient pose estimation. Our C-arm tracking algorithm estimates the pose of the C-arm with accuracy of 0.2°. The proposed C-arm calibration procedure allows the positioning of the C-arm within an error range of 0.5°. The resulting distortion correction leads to a mean pixel displacement of 0.30 pixel.

Index Terms — Distortion Correction, C-Arm Calibration, C-Arm Tracking, Pincushion Distortion, S-Distortion, C-Arm Motion Control

I. INTRODUCTION

X-ray image intensifiers are essential for surgeons to assess a patient’s anatomy and to guide their surgical instruments during minimally-invasive surgery. For automated guidance of robotic instruments in minimally-invasive procedures, it is crucial to obtain an accurate 3D shape estimation of the robots in real-time. Computed tomography (CT) as well as magnetic resonance imaging (MRI) are popular methods to reconstruct 3D volumes but these techniques are strongly limited by their relatively slow image acquisition times and their high costs. Therefore, it is desirable to facilitate image intensifiers to estimate the 3D shape of a minimally-invasive robot from a set of 2D projections. However, image intensifiers suffer from various kinds of distortions, limiting the direct application of their images for 3D reconstruction.

As described in [1], two main distortions occur in image intensifiers: Pincushion distortion and S-distortion. The projection of X-rays onto a curved input phosphor in the image intensifiers causes the pincushion distortion and makes objects at the periphery of the field of view appear bigger

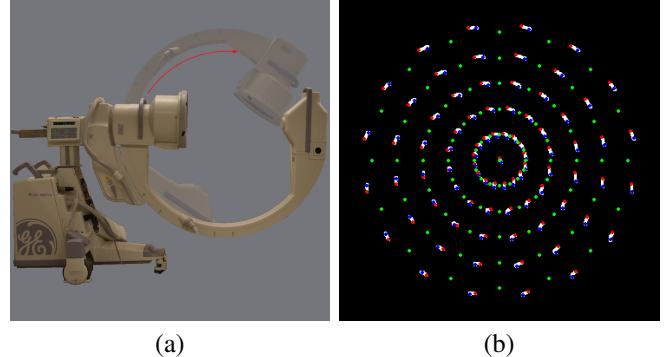


Fig. 1: (a) Typical orbital rotation of a C-arm; (b) The orientation-dependent distortion of a concentric calibration grid. The initial position of the C-arm in (a) corresponds to the red markers in (b) and the final position in (a) to the blue markers in (b). The green markers in (b) show the true and non-distorted positions of the points.

than structures in the center. Pincushion distortion is solely hardware-related and does not change as the orientation of the C-arm changes. The S-distortion occurs because of the interaction between accelerating electrons inside the image intensifier and an external magnetic field. Depending on the angle between the travel-direction of the electrons and the magnetic field, electrons deviate from their initial path, which leads to sinusoidal pattern in the resulting image. Unlike pincushion distortion, S-distortion strongly depends on the orientation of the image intensifier. Hence, it is necessary to take the orientation into consideration for correcting the distortion in an intensifier image. Fig. 1a shows the typical orbital motion of a C-arm. The impact of the C-arm pose on the resulting image is illustrated in Fig. 1b. As the image intensifier rotates, the points of the calibration grid in the image move away from the red markers until they reach the blue markers in the final position. This illustrates that the distortion occurring in X-ray images strongly depends on the orbital angle which must be considered for correcting the distortion. Based on these observations, we identified two main challenges: the accurate distortion correction of an image at a known angle and the precise tracking of a C-arm to obtain these angles.

For some applications, it is sufficient to only rectify the rotation-independent pincushion distortion. In [2] and [3], the radial error caused by the pincushion distortion was modeled by fitting a least-squares quadratic function, that minimizes the distance between the polynomial and known points on a calibration grid. Liu *et. al.* [4] also used a calibration

¹ Authors contributed equally to this work.

² Corresponding author (email: fheemeyer3@gatech.edu).

F. Heemeyer, A. Choudhary, and J. P. Desai are with the Medical Robotics and Automation Laboratory, Wallace H. Coulter Department of Biomedical Engineering, Georgia Institute of Technology, Atlanta, GA 30332 USA (e-mail: fheemeyer3@gatech.edu; achoudhary46@gatech.edu; jaydev@gatech.edu).

unit to extract the curvature of the input phosphor and correct the image geometrically. However, these approaches do not account for the orientation-dependent S-distortion. Navab *et. al.* [5] used a look-up table provided by the C-arm's vendor to rectify the S-distortion. The magnetic field deflecting the electrons in an image intensifier varies across different locations and cannot be limited to the earth's magnetic field [1]. Hence, the provided look-up tables do not provide sufficient accuracy for applications such as image reconstruction. Wang and Ning [6] described a local distortion correction algorithm wherein they individually rectified sub-images extracted from an X-ray image. The correction terms for all of the regions were estimated using a calibration grid. A similar approach is elaborated in [7]. Fahrig *et. al.* [8] captured 100 images at 2° steps and fit a fifth-order polynomial through pre-defined calibration points across all images. They linearly interpolated the coefficients between the two closest functions to correct images taken at arbitrary angles. Moreover, Gutierrez *et. al.* [9] developed a correction algorithm using 70 images to model the error across three degrees-of-freedom (DoFs).

Due to the frequent re-positioning during surgery as well as the orientation-dependent nature of the distortion, an accurate and reliable pose calibration of the C-arm is crucial. However, mechanical instability limits the accuracy of a C-arm's internal shape estimation and online tracking for C-arm pose estimation is required. Various approaches have been proposed for the real-time tracking of a C-arm using radiographic-fiducials [10], optical/electromagnetic trackers or external infrared/in-line cameras. Although some of these approaches achieved higher accuracy, the resultant configuration tends to be complex and interferes with the patient and clinical personnel. Optical tracking using infrared or motion-tracking with a stereo camera is a popular method using commercially available systems like OptoTrak and Polaris [11]. However, these approaches rely on markers which should be constantly in the field of view of the camera. It is difficult to ensure marker visibility in operating rooms due to the multiple orientations that C-arms can assume. An alternative approach uses electromagnetic sensors with a electromagnetic field generator mounted on the operating table [12], rendering the setup prone to error at extreme angles due to significant distortion caused by C-arm's X-ray signal in posterior-anterior position. Radiographic-fiducials have been used to estimate the orientation using a radio-opaque bead pattern, but it requires the bead pattern to be in the field of view of the C-arm as well as multiple X-ray images. Optical methods based on external cameras do not interfere with C-arm movement and impose negligible constraints. Keypoint correspondence across images is a strong constraint for pose estimation and has been extensively leveraged in computer vision for object tracking [13]. Jain and Fitchinger [14] highlighted that point correspondences across three rotational poses, can be used to perform sub-degree accurate pose estimation using weighted tripartite-matching. In previous studies, researchers have explored using C-arm-mounted as well as external camera-based tracking with

promising results. Reaungamornrat *et. al.* [15] developed an on-board optical system using a C-arm-mounted stereo camera for tracking a reference pattern on the operating table. They leveraged a commercial-grade video tracker achieving a sub-pixel level accuracy of $0.87 \text{ mm} \pm 0.25 \text{ mm}$. Wang *et. al.* [16] used a similar configuration for generating stitched X-ray panoramas by aligning the camera parallel to the X-ray beam and tracking a reference pattern placed near the patient. Amiri *et. al.* [17] developed a low cost on-board C-arm tracking system using inertial measurement units to measure orbital and tilt motions, along with laser distance sensors to measure up-down and in-out motions. Yet, the reliance of these approaches on markers or reference patterns limits their practicality. Hence, we rely on leveraging easily identifiable distinct C-arm components with an external camera-based setup and instead, focus on robust point-correspondence estimation to perform pose estimation.

In this work, we present an approach to correct the previously highlighted distortions caused by X-ray image intensifiers while simultaneously tracking the orientation of a C-arm. Section II-A summarizes the materials used for this work. In Section II-B, we introduce our novel C-arm tracking algorithm. In Section II-C, we use this tracking method to calibrate the motion control of a C-arm. The generation of the distortion correction term and how to facilitate it to correct a distorted X-ray image is described in Section II-D. Finally, in Section III, we present the results of the C-arm tracking, the C-arm calibration as well as the results of the distortion correction.

The key contributions of this work are as follows:

- 1) We use an external stereo camera setup to acquire images of a C-arm and estimate its pose using optical flow and point-correspondence based matching.
- 2) We propose an approach to calibrate the motion control of a C-arm based on the output of the C-arm pose estimation. This allows the precise rotation of a C-arm to any desired position.
- 3) We propose an integrated and highly accurate global curve fitting-based approach for C-arm distortion correction. Our approach models distortion as a function of C-arm orientation.

II. MATERIALS AND METHODS

A. Materials

In this work, the OEC 9800 Plus system by GE Healthcare is used for image acquisition and C-arm tracking. This C-arm has a resolution of $512 \text{ pixels} \times 512 \text{ pixels}$ and allows an orbital rotation of approximately 130° as shown in Fig. 1a. To retrieve the acquired images from the system, we set up a DICOM server using the Orthanc framework presented in [18]. We use the motion control interface by Imaging Systems & Service, Inc. to rotate the C-arm to the desired position. To track the C-arm, we facilitate a mobile phone camera (OnePlus 6), with known intrinsic parameters, in combination with the SuperPoint framework for keypoint extraction. For the estimation of the distortion

error, a concentric calibration grid of known geometry was manufactured. This calibration grid is a circular stainless steel plate with a hole in the center. As can be seen in Fig. 1b, 80 holes are arranged around the center with a radial distance of 5 cm and an angular distance of 22.5° between neighboring holes. The diameter of each hole is 1.8 mm.

B. C-Arm Pose Estimation

Given the feasibility challenges associated with marker and fiducial-based methods, we propose a simplistic camera-based configuration which can be easily generalized and used during a surgical procedure with minimal interference. Our tracking system uses a floor-mounted C-arm facing camera for estimating the angular pose of the C-arm. We leverage the fact that point-correspondences between images provides a good constraint for object pose estimation using homography matrix estimation. Although, commercially marker-based tracking systems can guarantee higher tracking accuracy, they enforce constraints on marker placement. In our research, we experimented with a MicronTracker stereo camera by ClaroNav but its detection accuracy suffered for larger distances between the C-arm and camera. Thus, we follow an alternative approach which does not rely on markers but instead leverages the X-ray assembly of C-arm using contextual feature descriptors for robust interest point detection and matching. Using the C-arm components has the benefit that it provides sufficient tracking points and is easily distinguishable from the background. Traditional keypoint matching approaches rely on estimating anchor points such as corners and learn associated descriptors using hand-crafted features. However, such approaches are prone to inconsistent anchor point estimation [19]. Recently, deep learning-based approaches attempt to identify and improve anchor point detection along with jointly learning the descriptor relying on traditional patch-based approach [20] [21] or full images [22] [23]. We leverage Superpoint [22], a self-supervised framework which operates on the complete image using a fully-convolutional network and jointly computes interest point locations and associated descriptors. It uses a single shared VGG-style encoder to learn image representation which is passed to decoders focusing on interest point detection and description. Furthermore, it uses self-supervised homographic transformation for improving the geometric consistency of keypoints and has been shown to produce denser and more accurate matches compared to patch-based approaches (LIFT [20], SIFT [24] and ORB [25]). We focus on tracking specific components of a C-arm, namely the image intensifier and X-ray emitter since they are not occluded by power-supplying wires which can exhibit unrelated motion. To track these components, we leverage holistic object representations [26] for object tracking along with the rotational motion. Motion is estimated using an unsupervised optical flow learning approach, given lack of training data and the limited generalization ability of supervised learning-based methods [27]. Conventional methods estimate optical flow using energy minimization [28], which is based on brightness constancy and spatial

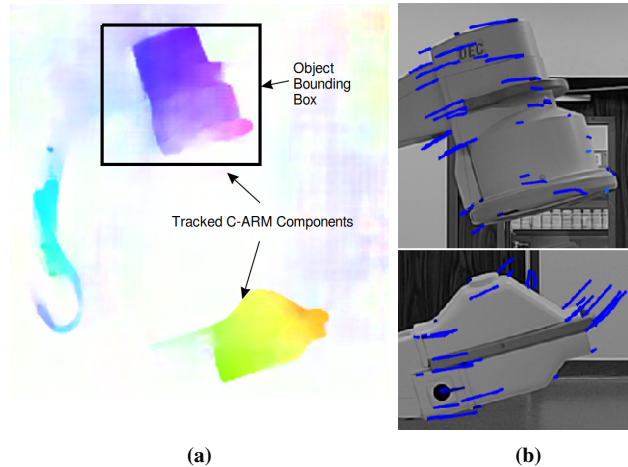


Fig. 2: Using the estimated optical flow (a), we derive a mask and superimpose over the original camera image to extract matching point correspondences between two orbital poses (b)

smoothness. However, such methods tend to fail under large displacements and they ignore temporal information over multiple frames. Recently, CNN-based optical flow approach relying on pyramidal warping estimation such as PWC-Net [29] has been shown to achieve higher accuracy. We leverage Selfflow [30], which integrates PWC-Net with self-supervised learning, to effectively integrate temporal information from multiple frames. Selfflow partitions the image into superpixels and performs bi-directional warping estimation using a coarse-to-fine approach along with imposing photometric loss, thereby achieving state-of-the-art results among unsupervised methods. We extract regions with higher optical flow using a velocity threshold, followed by morphological operations (erosion & dilation) to create a mask comprising C-arm's components to be tracked. Given two images, $I(\theta)$ and $I(\theta + r)$, acquired at two distinct orbital angles, we extract relevant C-arm regions for point-correspondence matching using optical flow derived masks. Using the Superpoint method, we extract keypoints along with descriptors and match them using nearest-neighbour matching from all interest points and descriptors detected in consecutive images using a descriptor L_2 -distance-based threshold (0.7). After finding the matched correspondences, we leverage RANSAC to estimate the homography matrix. Using the intrinsic parameters of the camera, we derive the rotation matrix from the homography matrix and estimate angular pose of the C-arm. We also pre-process our images using distortion correction and image normalization to derive more robust interest point descriptors.

C. Motion Calibration

The motion control of the C-arm suffers from relatively high inaccuracy with respect to the step sizes taken. We propose a calibration method based on the C-arm tracking approach presented in Section II-B to calibrate the C-arm motion control and allow precise positioning of the C-arm. The non-calibrated motion control is achieved by a proportional control scheme whereby the sensor readings

(acquired at approximately 14 Hz) are used to command the motion at the next time step. The velocity at which the C-arm rotates is a function of the distance between its current and the desired position. Due to the relatively low sample frequency and a momentum that acts on the C-arm even after the velocity is set to zero, the C-arm tends to overshoot its target position by a few degrees.

The main idea is to reach a target orientation taking a sequence of smaller calibrated steps. The C-arm can reach orientations ranging from 0° to 130° . To reach any position in this space within seven steps, we allow the following step sizes: 1° , 5° , 10° , 15° , 20° , 25° and 30° . The shortest sequence of steps to reach a goal is determined using Breadth-first search (BFS). A detailed description of BFS and how to implement it can be found in [31].

The input step size, μ_{input} , of the control system and the output step size, μ_{output} , which is obtained using the C-arm tracking approach presented in Section II-B, differ significantly. The relation between μ_{input} and μ_{output} can be described by a calibration coefficient, k_μ , leading to the following expression:

$$\mu_{output} = k_\mu \cdot \mu_{input} \quad (1)$$

To obtain k_μ for a certain step size, we take several measurements of that step size across the entire orientation space and calculate k_μ from the mean value of the measured μ_{output} using (1). The calculated k_μ is then used to determine the input step size, μ_{input} , that is needed to reach a desired step size, μ_{output} . This procedure is repeated for all step sizes that are used.

D. Distortion Correction

In this section, the distortion correction algorithm is presented where we correct a distorted image using a global curve, which is estimated by fitting a curve through points of several images of the calibration grid of known geometry.

As shown in Fig. 1b, the calibration grid consists of one center point and 80 points concentrically arranged around it. The grid is attached to the image intensifier in such a way that the center of the grid and the center of the image intensifier detector array coincide and that a known row is parallel to the detector array. The calibration grid was imaged in 258 different orientations ranging from 0° to 130° at approximately 0.5° increments. To map a point (x_{cor}, y_{cor}) in the corrected image to its corresponding point (x_{dis}, y_{dis}) in the distorted image, a distortion error function, $\epsilon = (\epsilon_x, \epsilon_y)$, is used, which leads to the following expressions:

$$x_{dis} = x_{cor} + \epsilon_x(x_{cor}, y_{cor}, \varphi) \quad (2)$$

$$y_{dis} = y_{cor} + \epsilon_y(x_{cor}, y_{cor}, \varphi) \quad (3)$$

where, φ , is the orbital angle at which the image is taken, (x_{cor}, y_{cor}) are the coordinates of the point in the corrected image, (x_{dis}, y_{dis}) are its corresponding coordinates in the distorted images, and (ϵ_x, ϵ_y) is the distortion error between

these points.

Hence, it is necessary to find expressions for the distortion errors, ϵ_x and ϵ_y , to properly correct a C-arm image. We estimate the distortion errors, $(\hat{\epsilon}_x$ and $\hat{\epsilon}_y)$, as polynomials of the form:

$$\hat{\epsilon}(x_{cor}, y_{cor}, \varphi) = \sum_{i=0}^m \sum_{j=0}^m \sum_{k=0}^n c_{ijk} x_{cor}^i y_{cor}^j \varphi^k \quad (4)$$

where m refers to the order of the polynomial in x - and y -direction and n to the order of the polynomial in φ -direction. c_{ijk} are constant coefficients that define the shape of the polynomial. In total, there are $N = (n+1) \cdot (m+1)^2$ coefficients characterizing the polynomial in Eq. (4).

From the 258 images of the calibration grid, the position of all points are detected using the blob detection in OpenCV. Since there is a total of 258 images and 81 points in each image, there are overall 20,898 points detected. Using Eqs. (2) and (3), the true distortion errors ϵ_x and ϵ_y for these 20,898 observations can thus be calculated. A general polynomial estimating the errors $\hat{\epsilon}_x$ and $\hat{\epsilon}_y$ is then derived by applying the polynomial regression algorithm to these points. All observation represent a linear system of M equations in the form of $Ax = b$:

$$A = \begin{bmatrix} (x_{cor,0}^0 y_{cor,0}^0 \varphi_0^0) & \dots & (x_{cor,0}^m y_{cor,0}^m \varphi_0^n) \\ (x_{cor,1}^0 y_{cor,1}^0 \varphi_1^0) & \dots & (x_{cor,1}^m y_{cor,1}^m \varphi_1^n) \\ \dots & \dots & \dots \\ \dots & \dots & \dots \\ (x_{cor,M}^0 y_{cor,M}^0 \varphi_M^0) & \dots & (x_{cor,M}^m y_{cor,M}^m \varphi_M^n) \end{bmatrix} \quad (5)$$

$$x = \begin{bmatrix} c_{000} \\ c_{001} \\ c_{002} \\ \dots \\ \dots \\ c_{nnm} \end{bmatrix} \quad (6) \qquad b = \begin{bmatrix} \epsilon_0 \\ \epsilon_1 \\ \epsilon_2 \\ \dots \\ \dots \\ \epsilon_M \end{bmatrix} \quad (7)$$

where m refers to the order of the polynomials in the x - and y -direction, n to the order of the polynomials in φ -direction and M to the total number of observations, which is 20,898.

The matrix, A , in Eq. (5) and the observation vector, b , in Eq. (7) are known. To find the solution vector, x_{sol} , in Eq. (6), the vector, x , minimizing the following expression must be found:

$$x_{sol} = \arg \min_{x \in \mathbb{R}^N} ||Ax - b||^2 + \lambda ||x||^2 \quad (8)$$

where λ refers to the regularization coefficient. The regularization term $\lambda ||x||^2$ levies a penalty for high coefficients in x , which leads to a smooth solution making it less sensitive to overfitting. Detailed procedures for solving least-square problems such as in Eq. (8) are described in [32], [33], and [34].

After the optimal solution, x_{sol} , for the vector, x , is computed, the values of c_{ijk} can be substituted into Eq. (4)

to estimate the distortion error for arbitrary points.

To correct an image taken at an angle, φ , an empty array with the size of the distorted image is initialized. The values for each pixel in this array are determined by finding its corresponding pixel in the distorted image and assigning its value to it. The corresponding pixel in the distorted image is found by using Eq. (2) and (3), with the estimated distortion errors $\hat{\epsilon}_x$ and $\hat{\epsilon}_y$ from Eq. (4) and the solution vector, x_{sol} , from Eq. (8) substituted into it. If the corresponding pixel location in the distorted image is not an integer, the correct value of the corresponding pixel is computed using bilinear interpolation between its four surrounding pixels.

III. RESULTS

In this section, the proposed approach is tested and its results are presented. First, the accuracy of the C-arm motion calibration is analyzed in Section III-A. Secondly, the accuracy of the distortion correction after the C-arm calibration at various angles is assessed in Section III-B. The goal is to eventually facilitate this approach to track a robotic guidewire. Therefore, we evaluate the algorithm's feasibility and potential to perform this task in Section III-C.

A. Pose Estimation and Motion Calibration

In this section, we investigate the accuracy of the C-arm's motion control. The accuracy of the proposed C-arm pose estimation algorithm was assessed by comparing the angles estimated by the camera to the manually-measured ground truth angles. The analysis showed that this method is able to track the C-arm pose with an accuracy of 0.2° . Following the method explained in Section II-C, the calibration coefficients were computed for each step size using the ground truth and camera-estimated angle values. A comparison of the calculated calibration coefficients is presented in Table I. Secondly, we used these coefficients to calibrate the C-arm motion control and evaluate the resulting positioning algorithm. To assess the accuracy of the resulting calibration, the C-arm was moved in certain step sizes, μ_{input} , and we computed the difference between the commanded motion and the output step size, μ_{output} , which was determined by manually measuring the true step size. The orientation error, φ_{error} , can be described as: $\varphi_{error} = |\mu_{output} - \mu_{input}|$. As shown in Fig. 3, the non-calibrated data shows significant motion errors for all step inputs. Through calibration, we achieve a mean error ranging from 0.05° for a step input of 1° to a 0.5° error for a step input of 30° . The precise motion not only leads to accurate distortion correction but will also help in performing 3D reconstruction and guidewire tracking with much higher confidence.

B. Distortion Correction

In this section, the accuracy of the proposed distortion correction approach with respect to the orbital orientation, φ , of the C-arm is analyzed. It is important that the distortion correction performs well at all possible orientations to enable it to be used for accurate image reconstruction. In most scenarios, the C-arm will be operated in orientations that

TABLE I: Comparison of the calibration coefficients for the motion control using camera-based tracking and the ground truth angles.

Step Input μ	$k_{\mu, camera}$	$k_{\mu, groundtruth}$
1°	1.029	1.028
5°	1.060	1.061
10°	1.068	1.077
15°	1.067	1.071
20°	1.068	1.078
25°	1.084	1.083
30°	1.062	1.079

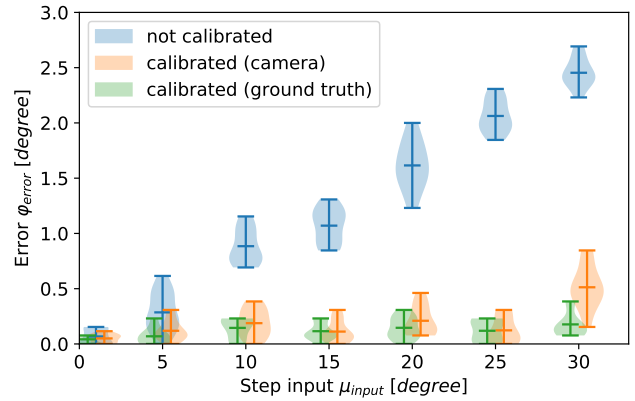


Fig. 3: True error of the C-arm motion control before calibration (blue) and after it is calibrated using the camera-based C-arm tracking (orange) and the ground truth (green). The green and orange violin plots are shifted -0.5° and 0.5° respectively to avoid an overlap of the plots.

have not been used to fit the global curve described in Section II-D. Hence, the accuracy at arbitrary angles is crucial for the representative assessment of the overall performance of the system. Out of the 258 images that were taken at 0.5° steps from 0° to 130° , every tenth image was used to evaluate the accuracy while the remaining images were used to estimate the polynomial. If the model performs well on these test images, it is a reasonable assumption that the model generalizes well and does not overfit to the training images. In Fig. 4, the performance of the distortion correction algorithm on the test data is shown across multiple C-arm orientations, φ . The displacement, $\Delta\epsilon$, of each point is calculated as follows:

$$\Delta\epsilon = \left\| \begin{pmatrix} \hat{\epsilon}_x - \epsilon_x \\ \hat{\epsilon}_y - \epsilon_y \end{pmatrix} \right\|_2 \quad (9)$$

where $\hat{\epsilon}_x$ and $\hat{\epsilon}_y$ refer to the estimated distortion error of a point and ϵ_x and ϵ_y to the true distortion error and $\|\cdot\|_2$ refers to the L_2 -norm of the vector. The overall mean displacement of all test images is 0.30 pixel, implying that each pixel is in average 0.30 pixel away from its true position. The blue plot shows the mean displacement at various angles. The true distortion errors, ϵ_x and ϵ_y , in the test images are extracted analogous to Section II-D and the estimated errors, $\hat{\epsilon}_x$ and $\hat{\epsilon}_y$, are computed using the trained model. The low deviation of the accuracy with respect to the angle, confirms that the presented method is a feasible way to model the distortion and to correct it at all possible orientations of the C-arm.

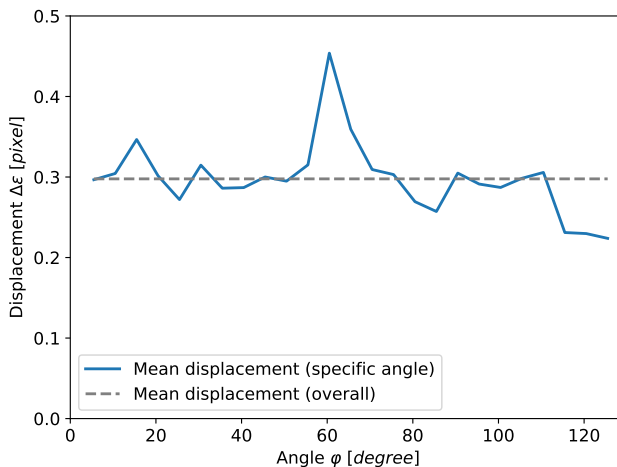


Fig. 4: This plot illustrates how the accuracy of the distortion correction on test data changes with respect to the orbital orientation, φ , of the C-arm. The blue line refers to the mean displacement of all pixels from their true position after distortion correction at a specific angle, φ . The dashed gray line shows the mean displacement over all angles.

C. Guidewire Tracking

A potential application of this approach is to precisely track a guidewire during a surgical procedure. We thus investigate our method's ability to correct a C-arm image of a guidewire at various orbital angles. To get an accurate estimation of the true location and shape of the guidewire, it is straightened and attached to the II perpendicularly to the detector array. Hence, it is known that the true guidewire should be horizontal and in a straight line in the center of the image. In Fig. 5, three C-arm orientations and the resulting images are shown. Analogous to Eq. (9), the displacement of a pixel on a guidewire is defined as its distance to its corresponding point on the true guidewire. Applying distortion correction, the mean displacement can be reduced from 20.67 pixels to 1.20 pixels performing equally well in all three cases. As discussed in Section II-D, the global curve is derived from images of the calibration unit. The high accuracy on the images of the guidewire emphasize the robustness of this approach and confirms that we can correct distortion in images other than the calibration grid as well.

IV. CONCLUSION

In this work, we presented an accurate and novel approach to correct for distortions in C-arm images. We estimate a global curve to determine the angle-dependent distortion correction term. The curve is modeled using polynomial regression on data points derived from 258 images that were acquired at different orbital orientations ranging from 0° to 130° . A C-arm tracking algorithm facilitating optical flow along with point-correspondence-based matching allows the accurate assessment of the current orientation of the C-arm. This tracking algorithm is then used to calibrate the motion control of the C-arm, which ensures the precise determination of the proper correction term. The proposed

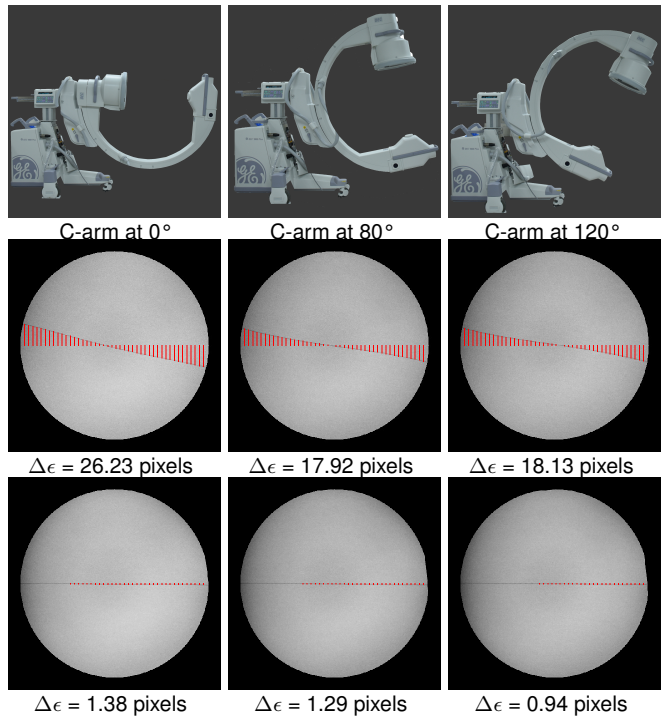


Fig. 5: This figure shows a C-arm in three different orientations (top row). The corresponding, distorted (middle row) and corrected (bottom row) images of a guidewire are shown below. The red lines in the images indicate the distance of a pixel on the guidewire to its true position. The mean displacement in the distorted images is 20.67 pixels. After distortion correction, the mean displacement decreases to 1.20 pixels.

method is able to track the C-arm with an accuracy of 0.2° and correct the distortion in C-arm images resulting in an mean displacement error of 0.30 pixel over all angles. However, this approach is limited to correcting images taken along the orbital axis. The roll motion of the C-arm can result in a faulty correction term and thus incorrect distortion correction. Therefore, in our future work we will extend this approach to more DoFs and thereby allow an accurate image reconstruction for the entire range of motion of the C-arm.

ACKNOWLEDGEMENT

Research reported in this publication was supported in part by the National Heart, Lung, And Blood Institute of the National Institutes of Health under Award Numbers R01HL144714 and R01HL140325. The content is solely the responsibility of the authors and does not necessarily represent the official views of the National Institutes of Health.

REFERENCES

- [1] T. C. Keating, D. D. Bohl, and K. S. Hamid, "A review of fluoroscopic image-intensifier artifacts and the next generation of isocentric c-arm imaging," *JBJS Reviews*, vol. 6, p. e4, Dec. 2018.
- [2] J. T. Hing, A. D. Brooks, and J. P. Desai, "A biplanar fluoroscopic approach for the measurement, modeling, and simulation of needle and soft-tissue interaction," *Medical Image Analysis*, vol. 11, pp. 62–78, Feb. 2007.

- [3] J. Hing, A. Brooks, and J. Desai, "Reality-based needle insertion simulation for haptic feedback in prostate brachytherapy," in *Proceedings 2006 IEEE International Conference on Robotics and Automation, 2006. ICRA 2006*, IEEE.
- [4] T. Liu, A. A. Malcolm, and J. Xu, "Pincushion distortion correction in x-ray imaging with an image intensifier," in *Fourth International Conference on Experimental Mechanics* (C. Quan, K. Qian, A. K. Asundi, and F. S. Chau, eds.), SPIE, Dec. 2009.
- [5] N. Navab, S.-M. Heining, and J. Traub, "Camera augmented mobile c-arm (CAMC): Calibration, accuracy study, and clinical applications," *IEEE Transactions on Medical Imaging*, vol. 29, pp. 1412–1423, July 2010.
- [6] X. Wang and R. Ning, "Accurate and efficient image-intensifier distortion-correction algorithm and its application in volume tomographic angiography," in *Medical Imaging 1997: Physics of Medical Imaging* (R. L. V. Metter and J. Beutel, eds.), SPIE, May 1997.
- [7] D. Soimu, C. Badea, and N. Pallikarakis, "A novel approach for distortion correction for x-ray image intensifiers," *Computerized Medical Imaging and Graphics*, vol. 27, pp. 79–85, Jan. 2003.
- [8] R. Fahrig, M. Moreau, and D. W. Holdsworth, "Three-dimensional computed tomographic reconstruction using a c-arm mounted XRII: Correction of image intensifier distortion," *Medical Physics*, vol. 24, pp. 1097–1106, July 1997.
- [9] L. F. Gutiérrez, C. Ozturk, E. R. McVeigh, and R. J. Lederman, "A practical global distortion correction method for an image intensifier based x-ray fluoroscopy system," *Medical Physics*, vol. 35, pp. 997–1007, Feb. 2008.
- [10] P. Fallavollita, E. Burdette, D. Y. Song, P. Abolmaesumi, and G. Fichtinger, "Unsupervised c-arm pose tracking with radiographic fiducial," *Medical physics*, vol. 38, no. 4, pp. 2241–2245, 2011.
- [11] NDigital Tracking Products. <https://www.ndigital.com/msci/products/>.
- [12] J. Yoo, S. Schafer, A. Uneri, Y. Otake, A. J. Khanna, and J. H. Siewerdsen, "An electromagnetic ‘tracker-in-table’ configuration for x-ray fluoroscopy and cone-beam ct-guided surgery," *International journal of computer assisted radiology and surgery*, vol. 8, no. 1, pp. 1–13, 2013.
- [13] K. Lenc and A. Vedaldi, "Large scale evaluation of local image feature detectors on homography datasets," *arXiv preprint arXiv:1807.07939*, 2018.
- [14] A. Jain and G. Fichtinger, "C-arm tracking and reconstruction without an external tracker," in *International Conference on Medical Image Computing and Computer-Assisted Intervention*, pp. 494–502, Springer, 2006.
- [15] S. Reaungamrat, Y. Otake, A. Uneri, S. Schafer, D. Mirota, S. Nithiananthan, J. Stayman, G. Kleinszig, A. Khanna, R. Taylor, and J. Siewerdsen, "An on-board surgical tracking and video augmentation system for c-arm image guidance," *International journal of computer assisted radiology and surgery*, vol. 7, pp. 647–65, 04 2012.
- [16] L. Wang, J. Traub, S. M. Heining, S. Benhimane, E. Euler, R. Graumann, and N. Navab, "Long bone x-ray image stitching using camera augmented mobile c-arm," in *Medical Image Computing and Computer-Assisted Intervention – MICCAI 2008* (D. Metaxas, L. Axel, G. Fichtinger, and G. Székely, eds.), (Berlin, Heidelberg), pp. 578–586, Springer Berlin Heidelberg, 2008.
- [17] S. Amiri, D. R. Wilson, B. A. Masri, and C. Anglin, "A low-cost tracked c-arm (tc-arm) upgrade system for versatile quantitative intraoperative imaging," *International Journal of Computer Assisted Radiology and Surgery*, vol. 9, pp. 695–711, 2013.
- [18] S. Jodogne, "The Orthanc ecosystem for medical imaging," *Journal of Digital Imaging*, vol. 31, pp. 341–352, Jun 2018.
- [19] G. Csürka, C. R. Dance, and M. Humenberger, "From handcrafted to deep local features," *arXiv preprint arXiv:1807.10254*, 2018.
- [20] K. M. Yi, E. Trulls, V. Lepetit, and P. Fua, "Lift: Learned invariant feature transform," in *European Conference on Computer Vision*, pp. 467–483, Springer, 2016.
- [21] N. Savinov, A. Seki, L. Ladicky, T. Sattler, and M. Pollefeys, "Quad-networks: Unsupervised learning to rank for interest point detection," *2017 IEEE Conference on Computer Vision and Pattern Recognition (CVPR)*, Jul 2017.
- [22] D. DeTone, T. Malisiewicz, and A. Rabinovich, "Superpoint: Self-supervised interest point detection and description," *2018 IEEE/CVF Conference on Computer Vision and Pattern Recognition Workshops (CVPRW)*, Jun 2018.
- [23] Y. Verdie, K. M. Yi, P. Fua, and V. Lepetit, "Tilde: A temporally invariant learned detector," *2015 IEEE Conference on Computer Vision and Pattern Recognition (CVPR)*, Jun 2015.
- [24] D. G. Lowe, "Distinctive image features from scale-invariant keypoints," *International journal of computer vision*, vol. 60, no. 2, pp. 91–110, 2004.
- [25] E. Rublee, V. Rabaud, K. Konolige, and G. R. Bradski, "Orb: An efficient alternative to sift or surf," in *ICCV*, vol. 11, p. 2, Citeseer, 2011.
- [26] A. Sauer, E. Aljalbout, and S. Haddadin, "Tracking holistic object representations," in *British Machine Vision Conference (BMVC)*, 2019.
- [27] J. Y. Jason, A. W. Harley, and K. G. Derpanis, "Back to basics: Unsupervised learning of optical flow via brightness constancy and motion smoothness," in *European Conference on Computer Vision*, pp. 3–10, Springer, 2016.
- [28] C. Zach, T. Pock, and H. Bischof, "A duality based approach for realtime tv-l 1 optical flow," in *Joint pattern recognition symposium*, pp. 214–223, Springer, 2007.
- [29] D. Sun, X. Yang, M.-Y. Liu, and J. Kautz, "Pwc-net: Cnn's for optical flow using pyramid, warping, and cost volume," *2018 IEEE/CVF Conference on Computer Vision and Pattern Recognition*, Jun 2018.
- [30] P. Liu, M. Lyu, I. King, and J. Xu, "Selfflow: Self-supervised learning of optical flow," 2019.
- [31] S. Russell and P. Norvig, *Artificial Intelligence: A Modern Approach*. Upper Saddle River, NJ, USA: Prentice Hall Press, 3rd ed., 2009.
- [32] J. Nocedal and S. J. Wright, *Numerical Optimization*. Springer New York, second ed., 2006.
- [33] M. Richter, *Inverse Problems*. Springer International Publishing, 2016.
- [34] C. Bauckhage, "Numpy / scipy recipes for data science: Regularized least squares optimization," 03 2015.